

1
2 **Tuning transcriptional regulation through signaling: A predictive theory**
3 **of allosteric induction**

4
5 **Manuel Razo-Mejia^{1,†}, Stephanie L. Barnes^{1,†}, Nathan M. Belliveau^{1,†}, Griffin Chure^{1,†},**
6 **Tal Einav^{2,†}, Mitchell Lewis³, Rob Phillips^{1,4,*}**

7 ¹Division of Biology and Biological Engineering, California Institute of Technology, Pasadena, CA,
8 United States; ²Department of Physics, California Institute of Technology, Pasadena, CA, United States;

9 ³Department of Biochemistry and Biophysics, University of Pennsylvania School of Medicine,
10 Philadelphia, PA, United States; ⁴Department of Applied Physics, California Institute of Technology,
11 Pasadena, CA, United States

12 † contributed equally

13 * phillips@pboc.caltech.edu

14 **Abstract**

15 Allosteric regulation is found across all domains of life, yet we still lack simple, predictive theories that
16 directly link the experimentally tunable parameters of a system to its input-output response. To that end,
17 we present a general theory of allosteric transcriptional regulation using the Monod-Wyman-Changeux
18 model. We rigorously test this model using the ubiquitous simple repression motif in bacteria by first
19 predicting the behavior of strains that span a large range of repressor copy numbers and DNA binding
20 strengths and then constructing and measuring their response. Our model not only accurately captures
21 the induction profiles of these strains but also enables us to derive analytic expressions for key properties
22 such as the dynamic range and $[EC_{50}]$. Finally, we derive an expression for the free energy of allosteric
23 repressors which enables us to collapse our experimental data onto a single master curve that captures
24 the diverse phenomenology of the induction profiles.

25 Introduction

26 Understanding how organisms sense and respond to changes in their environment has long been a central
27 theme of biological inquiry. At the cellular level, this interaction is mediated by a diverse collection
28 of molecular signaling pathways. A pervasive mechanism of signaling in these pathways is allosteric
29 regulation, in which the binding of a ligand induces a conformational change in some target molecule,
30 triggering a signaling cascade [1]. One of the most important examples of such signaling is offered by
31 transcriptional regulation, where a transcription factor's propensity to bind to DNA will be altered upon
32 binding to an allosteric effector.

33 Despite the overarching importance of this mode of signaling, a quantitative understanding of
34 the molecular interactions between extracellular inputs and gene expression remains poorly explored.
35 Attempts to reconcile theoretical models and experiments have often been focused on fitting data
36 retrospectively after experiments have been conducted [2, 3]. Further, many treatments of induction are
37 strictly phenomenological, electing to treat induction curves individually either using Hill functions or
38 as ratios of polynomials without acknowledging that allosteric proteins have distinct conformational
39 states depending upon whether an effector molecule is bound to them or not [4–8]. These fits are
40 made in experimental conditions in which there is great uncertainty about the copy number of both the
41 transcription factor and the regulated locus, meaning that the underlying minimal set of parameters
42 cannot be pinned down unequivocally. This leaves little prospect for predicting or understanding what
43 molecular properties determine key phenotypic parameters such as leakiness, dynamic range, $[EC_{50}]$, and
44 the effective Hill coefficient as discussed in Refs. [9, 10] and illustrated in Fig. 1. Our goal was to use a
45 minimal Monod-Wyman-Changeux (MWC) model of transcription factor induction in conjunction with
46 a corresponding thermodynamic model of repression to test whether such a simple model is capable of
47 predicting how the induction process changes over broad swathes of regulatory parameter space. While
48 some treatments of induction have used MWC models to predict transcriptional outputs [3, 11, 12], these
49 often require multi-parameter fitting which gives rise to issues of parameter degeneracy (see Appendix A)
50 and may include effective parameters that have tenuous biological meaning. In contrast, our objective
51 was to use the MWC model to make parameter-free predictions about how the induction response will
52 be altered when transcription factor copy number and operator strength are systematically varied.

53 We test our model in the context of the simple repression motif – a widespread bacterial genetic
54 regulatory architecture in which binding of a transcription factor occludes binding of an RNA polymerase
55 thereby inhibiting transcription initiation. A recent survey of different regulatory architectures within the
56 *E. coli* genome revealed that more than 100 genes are characterized by the simple repression motif, making
57 it a common and physiologically relevant architecture [13]. Building upon previous work [14–16], we
58 present a statistical mechanical rendering of allostery in the context of induction and corepression, shown
59 schematically in Fig. 1A, and use this model as the basis of parameter-free predictions which we then
60 probe experimentally. Specifically, we model the allosteric response of transcriptional repressors using the
61 MWC model, which stipulates that an allosteric protein fluctuates between two distinct conformations –
62 an active and inactive state – in thermodynamic equilibrium [17]. In the context of induction, effector
63 binding increases the probability that a repressor will be in the inactive state, weakening its ability to
64 bind to the promoter and resulting in increased expression. The framework presented here provides
65 considerable insight beyond that of simply fitting a sigmoidal curve to inducer titration data. We
66 aim to explain and predict the relevant biologically important parameters of an induction profile, such
67 as characterizing the midpoint and steepness of its response as well as the limits of minimum and
68 maximum expression as shown in Fig. 1B. By combining this MWC treatment of induction with a
69 thermodynamic model of transcriptional regulation (Fig. 2), we create a general quantitative model of
70 allosteric transcriptional regulation that is applicable to a wide range of regulatory architectures such as
71 activation, corepression, and various combinations thereof, extending our quantitative understanding of
72 these schemes [18] to include signaling.

73 To demonstrate the predictive power of our theoretical formulation across a wide range of both
74 operator strengths and repressor copy numbers, we design an *E. coli* genetic construct in which the
75 binding probability of a repressor regulates gene expression of a fluorescent reporter. Using components
76 from the well-characterized *lac* system in *E. coli*, we first quantify the three parameters associated with

77 the induction of the repressor, namely, the binding affinity of the active and inactive repressor to the
78 inducer and the free energy difference between the active and inactive repressor states. We determine
79 these parameters by fitting to measurements of the fold-change in gene expression as a function of inducer
80 concentration for a circuit with known repressor copy number and repressor-operator binding energy. We
81 note that all other parameters that appear in the thermodynamic model are used without change from a
82 suite of earlier experiments which quantify fold-change in a range of regulatory scenarios [14, 15, 19–22].
83 With these estimated allosteric parameters in hand, we make accurate, parameter-free predictions of the
84 induction response for many other combinations of repressor copy number and binding energy. This goes
85 well beyond previous treatments of the induction phenomenon and shows that one extremely compact set
86 of parameters can be applied self-consistently and predictively to vastly different regulatory situations
87 including simple repression on chromosome, cases in which decoy binding sites for repressor are put on
88 plasmids, cases in which multiple genes compete for the same regulatory machinery, cases involving
89 multiple binding sites for repressor leading to DNA looping, and the induction experiments described
90 here. The broad reach of this minimal parameter set is highlighted in Fig. 3.

91 Rather than viewing the behavior of each circuit as giving rise to its own unique input-output response,
92 the formulation of the MWC model presented here provides a means to characterize these seemingly
93 diverse behaviors using a single unified framework governed by a small set of parameters, applicable even
94 to mutant repressors in much the same way that earlier work showed how mutants in quorum sensing
95 and chemotaxis receptors could be understood within a minimal MWC-based model [23, 24]. Another
96 insight that emerges from our theoretical treatment is how a subset in the parameter space of repressor
97 copy number, operator binding site strength, and inducer concentration can all yield the same level
98 of gene expression. Our application of the MWC model allows us to understand these degeneracies in
99 parameter space through an expression for the free energy of repressor binding, a nonlinear combination
100 of physical parameters which determines the system’s mean response and is the fundamental quantity
101 that dictates the phenotypic cellular response to a signal.

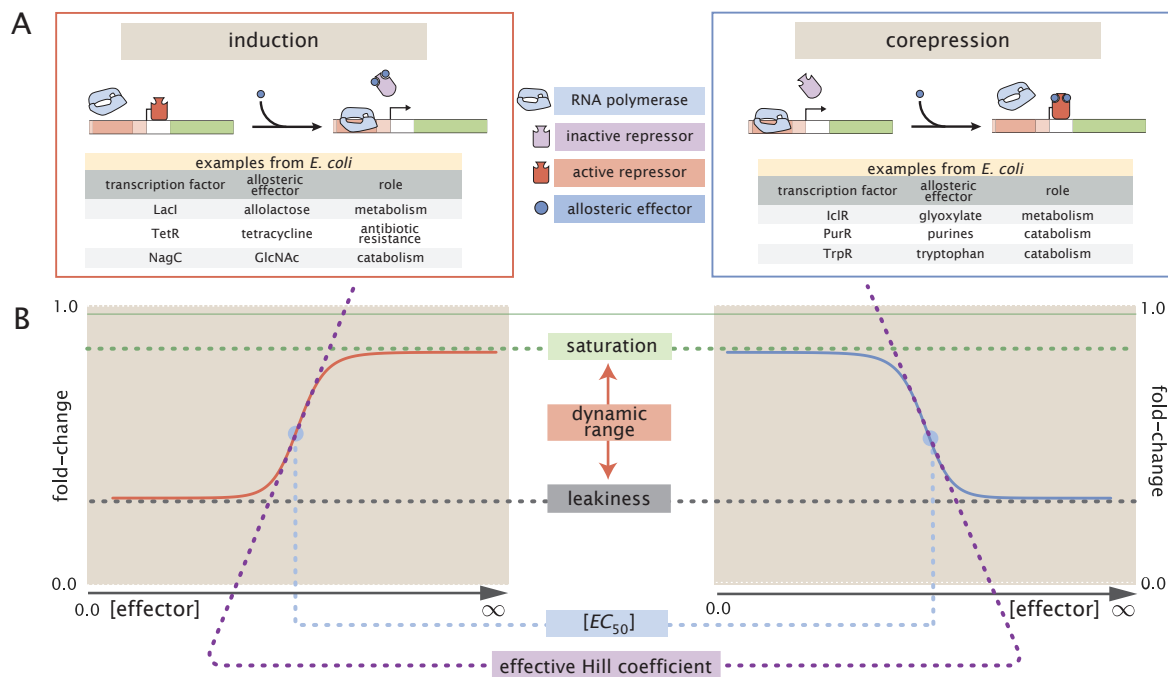


Figure 1. Transcription regulation architectures involving an allosteric repressor. (A) We consider a promoter regulated solely by an allosteric repressor. When bound, the repressor prevents RNAP from binding and initiating transcription. Induction is characterized by the addition of an effector which binds to the repressor and stabilizes the inactive state (defined as the state which has a low affinity for DNA), thereby increasing gene expression. In corepression, the effector stabilizes the repressor’s active state and thus further reduces gene expression. We list several characterized examples of induction and corepression that support different physiological roles in *E. coli* [25,26]. (B) A schematic regulatory response of the two architectures shown in Panel A plotting the fold-change in gene expression as a function of effector concentration, where fold-change is defined as the ratio of gene expression in the presence versus the absence of repressor. We consider the following key phenotypic properties that describe each response curve: the minimum response (leakiness), the maximum response (saturation), the difference between the maximum and minimum response (dynamic range), the concentration of ligand which generates a fold-change halfway between the minimal and maximal response ($[EC_{50}]$), and the log-log slope at the midpoint of the response (effective Hill coefficient).

102 Results

103 Characterizing Transcription Factor Induction using the Monod-Wyman-Changeux 104 (MWC) Model

105 We begin by considering the induction of a simple repression genetic architecture, in which the binding of
106 a transcriptional repressor occludes the binding of RNA polymerase (RNAP) to the DNA [27, 28]. When
107 an effector (hereafter referred to as an “inducer” for the case of induction) binds to the repressor, it shifts
108 the repressor’s allosteric equilibrium towards the inactive state as specified by the MWC model [17].
109 This causes the repressor to bind more weakly to the operator, which increases gene expression. Simple
110 repression motifs in the absence of inducer have been previously characterized by an equilibrium model
111 where the probability of each state of repressor and RNAP promoter occupancy is dictated by the
112 Boltzmann distribution [14, 15, 27–30] (we note that non-equilibrium models of simple repression have
113 been shown to have the same functional form that we derive below [31]). We extend these models to
114 consider the role of allostery by accounting for the equilibrium state of the repressor through the MWC
115 model as follows.

116 Consider a cell with copy number P of RNAP and R repressors. Our model assumes that the repressor
117 can exist in two conformational states. R_A repressors will be in the active state (the favored state when
118 the repressor is not bound to an inducer; in this state the repressor binds tightly to the DNA) and the
119 remaining R_I repressors will be in the inactive state (the predominant state when repressor is bound to
120 an inducer; in this state the repressor binds weakly to the DNA) such that $R_A + R_I = R$. Repressors
121 fluctuate between these two conformations in thermodynamic equilibrium [17].

122 Thermodynamic models of gene expression begin by enumerating all possible states of the promoter
123 and their corresponding statistical weights. As shown in Fig. 2A, the promoter can either be empty,
124 occupied by RNAP, or occupied by either an active or inactive repressor. We assign the repressor a
125 different DNA binding affinity in the active and inactive state. In addition to the specific binding sites
126 at the promoter, we assume that there are N_{NS} non-specific binding sites elsewhere (i.e. on parts of the
127 genome outside the simple repression architecture) where the RNAP or the repressor can bind. All specific
128 binding energies are measured relative to the average non-specific binding energy. Our model explicitly
129 ignores the complexity of the distribution of non-specific binding affinities in the genome, and makes the
130 assumption that a single parameter can capture the energy difference between our binding site of interest
131 and the average site in the reservoir. Thus, $\Delta\varepsilon_P$ represents the energy difference between the specific
132 and non-specific binding for RNAP to the DNA. Likewise, $\Delta\varepsilon_{RA}$ and $\Delta\varepsilon_{RI}$ represent the difference in
133 specific and non-specific binding energies for repressor in the active or inactive state, respectively.


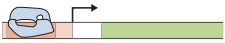


134 Thermodynamic models of transcription [2, 11, 14–16, 18, 27–30] posit that gene expression is propor-
135 tional to the probability that the RNAP is bound to the promoter p_{bound} , which is given by

$$p_{\text{bound}} = \frac{\frac{P}{N_{NS}} e^{-\beta\Delta\varepsilon_P}}{1 + \frac{R_A}{N_{NS}} e^{-\beta\Delta\varepsilon_{RA}} + \frac{R_I}{N_{NS}} e^{-\beta\Delta\varepsilon_{RI}} + \frac{P}{N_{NS}} e^{-\beta\Delta\varepsilon_P}}, \quad (1)$$

136 with $\beta = \frac{1}{k_B T}$ where k_B is the Boltzmann constant and T is the temperature of the system. As $k_B T$ is
137 the natural unit of energy at the molecular length scale, we treat the products $\beta\Delta\varepsilon_j$ as single parameters
138 within our model. Measuring p_{bound} directly is fraught with experimental difficulties, as determining
139 the exact proportionality between expression and p_{bound} is not straightforward. Instead, we measure
140 the fold-change in gene expression due to the presence of the repressor. We define fold-change as the
141 ratio of gene expression in the presence of repressor relative to expression in the absence of repressor (i.e.
142 constitutive expression), namely,

$$\text{fold-change} \equiv \frac{p_{\text{bound}}(R > 0)}{p_{\text{bound}}(R = 0)}. \quad (2)$$

143 We can simplify this expression using two well-justified approximations: (1) $\frac{P}{N_{NS}} e^{-\beta\Delta\varepsilon_P} \ll 1$ implying
144 that the RNAP binds weakly to the promoter ($N_{NS} = 4.6 \times 10^6$, $P \approx 10^3$ [32], $\Delta\varepsilon_P \approx -2$ to $-5 k_B T$ [20],

A	description	state	statistical weight
	empty promoter		1
	RNA polymerase bound		$\frac{P}{N_{NS}} e^{-\beta \Delta \varepsilon_P}$
	active repressor bound		$\frac{R_A}{N_{NS}} e^{-\beta \Delta \varepsilon_{RA}}$
	inactive repressor bound		$\frac{R_I}{N_{NS}} e^{-\beta \Delta \varepsilon_{RI}}$




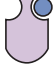

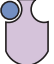

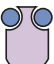
B	active		inactive	
	state	statistical weight	state	statistical weight
		1		$e^{-\beta \Delta \varepsilon_{AI}}$
		$\frac{c}{K_A}$		$e^{-\beta \Delta \varepsilon_{AI}} \frac{c}{K_I}$
		$\frac{c}{K_A}$		$e^{-\beta \Delta \varepsilon_{AI}} \frac{c}{K_I}$
		$\left(\frac{c}{K_A}\right)^2$		$e^{-\beta \Delta \varepsilon_{AI}} \left(\frac{c}{K_I}\right)^2$
	$\sum_{\text{active}} w_a = \left(1 + \frac{c}{K_A}\right)^2$		$\sum_{\text{inactive}} w_i = e^{-\beta \Delta \varepsilon_{AI}} \left(1 + \frac{c}{K_I}\right)^2$	

Figure 2. States and weights for the simple repression motif. (A) RNAP (light blue) and a repressor compete for binding to a promoter of interest. There are R_A repressors in the active state (red) and R_I repressors in the inactive state (purple). The difference in energy between a repressor bound to the promoter of interest versus another non-specific site elsewhere on the DNA equals $\Delta \varepsilon_{RA}$ in the active state and $\Delta \varepsilon_{RI}$ in the inactive state; the P RNAP have a corresponding energy difference $\Delta \varepsilon_P$ relative to non-specific binding on the DNA. N_{NS} represents the number of non-specific binding sites for both RNAP and repressor. (B) A repressor has an active conformation (red, left column) and an inactive conformation (purple, right column), with the energy difference between these two states given by $\Delta \varepsilon_{AI}$. The inducer (blue circle) at concentration c is capable of binding to the repressor with dissociation constants K_A in the active state and K_I in the inactive state. The eight states for a dimer with $n = 2$ inducer binding sites are shown along with the sums of the active and inactive states.

145 so that $\frac{P}{N_{NS}}e^{-\beta\Delta\varepsilon_P} \approx 0.01$) and (2) $\frac{R_I}{N_{NS}}e^{-\beta\Delta\varepsilon_{RI}} \ll 1 + \frac{R_A}{N_{NS}}e^{-\beta\Delta\varepsilon_{RA}}$ which reflects our assumption
 146 that the inactive repressor binds weakly to the promoter of interest. Using these approximations, the
 147 fold-change reduces to the form

$$\text{fold-change} \approx \left(1 + \frac{R_A}{N_{NS}}e^{-\beta\Delta\varepsilon_{RA}}\right)^{-1} \equiv \left(1 + p_A(c)\frac{R}{N_{NS}}e^{-\beta\Delta\varepsilon_{RA}}\right)^{-1}, \quad (3)$$

148 where in the last step we have introduced the fraction $p_A(c)$ of repressors in the active state given
 149 a concentration c of inducer, which is defined as $R_A(c) = p_A(c)R$. Since inducer binding shifts the
 150 repressors from the active to the inactive state, $p_A(c)$ is a decreasing function of c [10].

151 We compute the probability $p_A(c)$ that a repressor with n inducer binding sites will be active using
 152 the MWC model. After first enumerating all possible configurations of a repressor bound to inducer (see
 153 Fig. 2B), $p_A(c)$ is given by the sum of the weights of the active states divided by the sum of the weights
 154 of all possible states, namely,

$$p_A(c) = \frac{\left(1 + \frac{c}{K_A}\right)^n}{\left(1 + \frac{c}{K_A}\right)^n + e^{-\beta\Delta\varepsilon_{AI}}\left(1 + \frac{c}{K_I}\right)^n}, \quad (4)$$

155 where K_A and K_I represent the dissociation constant between the inducer and repressor in the active
 156 and inactive states, respectively, and $\Delta\varepsilon_{AI} = \varepsilon_I - \varepsilon_A$ stands for the free energy difference between a
 157 repressor in the inactive and active state (the quantity $e^{-\Delta\varepsilon_{AI}}$ is sometimes denoted by L [10, 17] or
 158 K_{RR^*} [11]). A repressor which favors the active state in the absence of inducer ($\Delta\varepsilon_{AI} > 0$) will be driven
 159 towards the inactive state upon inducer binding when $K_I < K_A$. The specific case of a repressor dimer
 160 with $n = 2$ inducer binding sites is shown in Fig. 2B.

161 Substituting $p_A(c)$ from Eq. (4) into Eq. (3) yields the general formula for induction of a simple
 162 repression regulatory architecture, namely,

$$\text{fold-change} = \left(1 + \frac{\left(1 + \frac{c}{K_A}\right)^n}{\left(1 + \frac{c}{K_A}\right)^n + e^{-\beta\Delta\varepsilon_{AI}}\left(1 + \frac{c}{K_I}\right)^n} \frac{R}{N_{NS}}e^{-\beta\Delta\varepsilon_{RA}}\right)^{-1}. \quad (5)$$

163 While we have used the specific case of simple repression with induction to craft this model, we reiterate
 164 that the exact same mathematics describe the case of corepression in which binding of an allosteric effector
 165 stabilizes the active state of the repressor and decreases gene expression (see Fig. 1B). Interestingly, we
 166 shift from induction (governed by $K_I < K_A$) to corepression ($K_I > K_A$) as the ligand transitions from
 167 preferentially binding to the inactive repressor state to stabilizing the active state. Furthermore, this
 168 general approach can be used to describe a variety of other motifs such as activation, multiple repressor
 169 binding sites, and combinations of activator and repressor binding sites [15, 16, 18].

170 This key formula presented in Eq. (5) enables us to make precise quantitative statements about
 171 induction profiles. Motivated by the broad range of predictions implied by this equation, we designed
 172 a series of experiments using the *lac* system in *E. coli* to tune the control parameters for a simple
 173 repression genetic circuit. As discussed in Fig. 3, previous studies from our lab have provided us with
 174 well-characterized values for many of the parameters in our experimental system, leaving only the values
 175 of the the MWC parameters (K_A , K_I , and $\Delta\varepsilon_{AI}$) to be determined. We note that while previous
 176 studies have obtained values for K_A , K_I , and $L = e^{-\beta\Delta\varepsilon_{AI}}$ [11, 33], they were either based upon clever
 177 biochemical experiments or *in vivo* conditions involving poorly characterized transcription factor copy
 178 numbers and gene copy numbers. These differences relative to our experimental conditions and fitting
 179 techniques led us to believe that it was important to perform our own analysis of these parameters.
 180 Indeed, after inferring these three MWC parameters (see Appendix A for details regarding the inference of
 181 $\Delta\varepsilon_{AI}$, which was fitted separately from K_A and K_I), we were able to predict the input/output response
 182 of the system under a broad range of experimental conditions. For example, this framework can predict
 183 the response of the system at different repressor copy numbers R , repressor-operator affinities $\Delta\varepsilon_{RA}$,
 184 inducer concentrations c , and gene copy numbers (see Appendix B).

185 Experimental Design

186 To test this model of allostery, we build off of a collection of work that has developed both a quantitative
 187 understanding of and experimental control over the simple repression motif. As shown in Fig. 3, earlier
 188 work from our laboratory used *E. coli* constructs based on components of the *lac* system to demonstrate
 189 how the Lac repressor (LacI) copy number R and operator binding energy $\Delta\varepsilon_{RA}$ affect gene expression
 190 in the absence of inducer [14]. Rydenfelt *et al.* [34] extended the theory used in that work to the case of
 191 multiple promoters competing for a given transcription factor, which was demonstrated experimentally
 192 by Brewster *et al.* [15], who modified this system to consider expression from multiple-copy plasmids as
 193 well as the presence of competing repressor binding sites. Although the current work focuses on systems
 194 with a single site of repression, in Appendix A we utilize data from Brewster *et al.* [15] to characterize
 195 the allosteric free energy difference $\Delta\varepsilon_{AI}$ between the repressor's active and inactive states. With this
 196 parameter in hand, the present work considers the effects of an inducer on gene expression, adding yet
 197 another means for tuning the behavior of the system. A remarkable feature of our approach is how
 198 accurately our simple model quantitatively describes the mean response of a wide variety of regulatory
 199 contexts. We extend this body of work by introducing three additional biophysical parameters – $\Delta\varepsilon_{AI}$,
 200 K_A , and K_I – which capture the allosteric nature of the transcription factor and complement the results
 201 shown by Garcia and Phillips [14] and Brewster *et al.* [15].

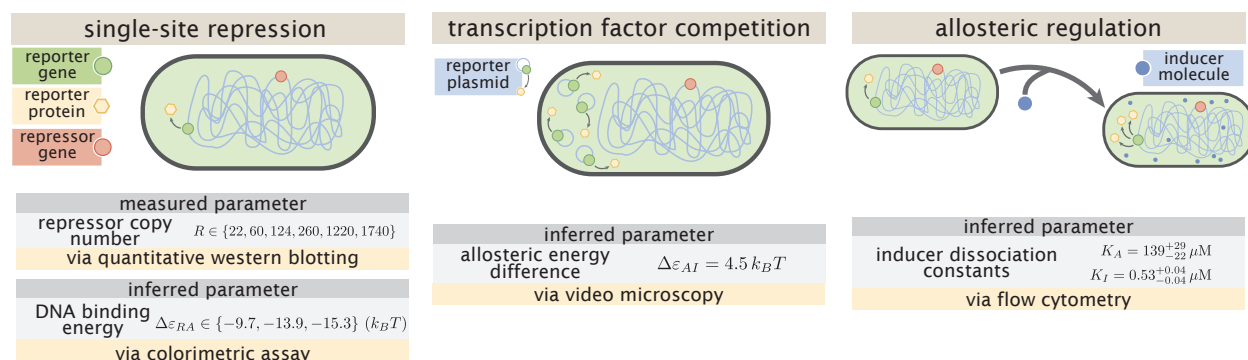


Figure 3. Understanding the modular components of induction. Over the past decade, we have refined both our experimental control over and theoretical understanding of the simple repression architectures. A first round of experiments used colorimetric assays and quantitative Western blots to investigate how single-site repression is modified by the repressor copy number and repressor-DNA binding energy [14]. A second round of experiments used video microscopy to probe how the copy number of the promoter and presence of competing repressor binding sites affect gene expression, and we use this data set to determine the free energy difference between the repressor's inactive and active conformations [15] (see Appendix A). Both of the previous experiments characterized the system in the absence of an inducer, and in the present work we consider this additional important feature of the simple repression architecture. We used flow cytometry to determine the inducer-repressor dissociation constants and demonstrate that with these parameters we can predict *a priori* the behavior of the system for any repressor copy number, DNA binding energy, gene copy number, and inducer concentration.

202 To test this extension to the theory of transcriptional regulation by simple repression, we predicted the
 203 induction profiles for an array of strains that could be made using the previously characterized repressor
 204 copy number and DNA binding energies. More specifically, we used modified *lacI* ribosomal binding sites
 205 from Garcia and Phillips [14] to generate strains with mean repressor copy number per cell of $R = 22 \pm 4$,
 206 60 ± 20 , 124 ± 30 , 260 ± 40 , 1220 ± 160 , and 1740 ± 340 , where the error denotes standard deviation of
 207 at least three replicates as measured by Garcia and Phillips [14]. We note that repressor copy number R
 208 refers to the number of repressor dimers in the cell, which is twice the number of repressor tetramers
 209 reported by Garcia and Phillips [14]; since both heads of the repressor are assumed to always be either
 210 specifically or non-specifically bound to the genome, the two repressor dimers in each LacI tetramer can
 211 be considered independently. Gene expression was measured using a Yellow Fluorescent Protein (YFP)

212 gene, driven by a *lacUV5* promoter. Each of the six repressor copy number variants were paired with the
213 native O1, O2, or O3 LacI operator [35] placed at the YFP transcription start site, thereby generating
214 eighteen unique strains. The repressor-operator binding energies (O1 $\Delta\varepsilon_{RA} = -15.3 \pm 0.2 k_B T$, O2
215 $\Delta\varepsilon_{RA} = -13.9 k_B T \pm 0.2$, and O3 $\Delta\varepsilon_{RA} = -9.7 \pm 0.1 k_B T$) were previously inferred by measuring the
216 fold-change of the *lac* system at different repressor copy numbers, where the error arises from model
217 fitting [14]. Additionally, we were able to obtain the value $\Delta\varepsilon_{AI} = 4.5 k_B T$ by fitting to previous data
218 as discussed in Appendix A. We measure fold-change over a range of known IPTG concentrations c ,
219 using $n = 2$ inducer binding sites per LacI dimer and approximating the number of non-specific binding
220 sites as the length in base-pairs of the *E. coli* genome, $N_{NS} = 4.6 \times 10^6$. We proceed by first inferring
221 the values of the repressor-inducer dissociation constants K_A and K_I using Bayesian inferential methods
222 as discussed below [36]. When combined with the previously measured parameters within Eq. (5), this
223 enables us to predict gene expression for any concentration of inducer, repressor copy number, and DNA
224 binding energy.

225 Our experimental pipeline for determining fold-change using flow cytometry is shown in Fig. 4.
226 Briefly, cells were grown to exponential phase, in which gene expression reaches steady state [37], under
227 concentrations of the inducer IPTG ranging between 0 and 5 mM. We measure YFP fluorescence using
228 flow cytometry and automatically gate the data to include only single-cell measurements (see Appendix
229 C). To validate the use of flow cytometry, we also measured the fold-change of a subset of strains using
230 the established method of single-cell microscopy (see Appendix D). We found that the fold-change
231 measurements obtained from microscopy were indistinguishable from that of flow-cytometry and yielded
232 values for the inducer binding constants K_A and K_I that were within error.

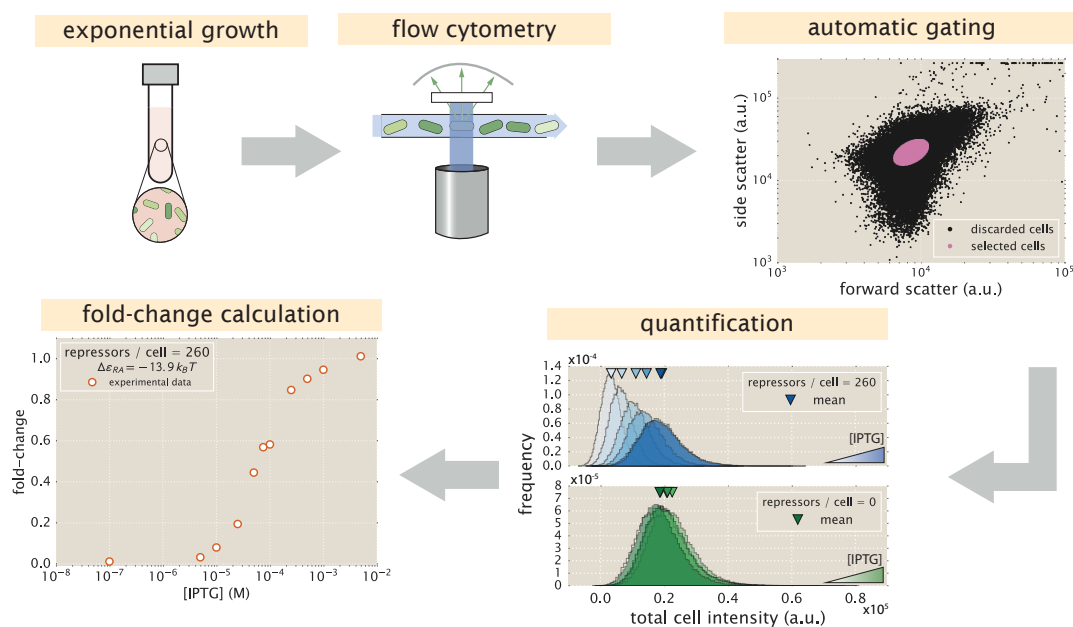


Figure 4. An experimental pipeline for high-throughput fold-change measurements. Cells are grown to exponential steady state and their fluorescence is measured using flow cytometry. Automatic gating methods using forward- and side-scattering are used to ensure that all measurements come from single cells (see Methods). Mean expression is then quantified at different IPTG concentrations (top, blue histograms) and for a strain without repressor (bottom, green histograms), which shows no response to IPTG as expected. Fold-change is computed by dividing the mean fluorescence in the presence of repressor by the mean fluorescence in the absence of repressor.

233 Determination of the *in vivo* MWC Parameters

234 The three parameters that we tune experimentally are shown in Fig. 5A, leaving the three allosteric
235 parameters ($\Delta\varepsilon_{AI}$, K_A , and K_I) to be determined by fitting. Using previous LacI fold-change data [15],
236 we infer that $\Delta\varepsilon_{AI} = 4.5 k_B T$ (see Appendix A). Rather than fitting K_A and K_I to our entire data set
237 of eighteen unique constructs, we performed a Bayesian parameter estimation on the data from a single
238 strain with $R = 260$ and an O2 operator ($\Delta\varepsilon_{RA} = -13.9 k_B T$ [14]) shown in Fig. 5D (white circles). Using
239 Markov Chain Monte Carlo, we determine the most likely parameter values to be $K_A = 139_{-22}^{+29} \times 10^{-6}$ M
240 and $K_I = 0.53_{-0.04}^{+0.04} \times 10^{-6}$ M, which are the modes of their respective distributions, where the superscripts
241 and subscripts represent the upper and lower bounds of the 95th percentile of the parameter value
242 distributions as depicted in Fig. 5B. Unfortunately, we are not able to make a meaningful value-for-
243 value comparison of our parameters to those of earlier studies [3, 11] because of the effects induced by
244 uncertainties in both gene copy number and transcription factor numbers, the importance of which is
245 illustrated by the plots in Appendix B. To demonstrate the strength of our parameter-free model, we
246 then predicted the fold-change for the remaining seventeen strains with no further fitting (see Fig. 5C-E)
247 together with the specific phenotypic properties described in Fig. 1 and discussed in detail below (see
248 Fig. 5F-J). The shaded regions in Fig. 5C-J denote the 95% credible regions. An interesting aspect of
249 our predictions of fold-change is that the width of the credible regions increases with repressor copy
250 number and inducer concentration but decreases with the repressor-operator binding strength. Note that
251 the fold-change Eq. (5) depends on the product of $\frac{R}{N_{NS}} e^{-\beta\Delta\varepsilon_{RA}}$ with the MWC parameters K_A , K_I ,
252 and $\Delta\varepsilon_{AI}$. As a result, strains with small repressor copy numbers, as well as strains with weak binding
253 energies such as O3, will necessarily suppress variation in the MWC parameters (see Appendix E).

254 We stress that the entire suite of predictions in Fig. 5 is based upon the induction profile of a single
255 strain. Our ability to make such a broad range of predictions stems from the fact that our parameters
256 of interest - such as the repressor copy number and DNA binding energy - appear as distinct physical
257 parameters within our model. While the single data set in Fig. 5D could also be fit using a Hill function,
258 such an analysis would be unable to predict any of the other curves in the figure. Phenomenological
259 expressions such as the Hill function can describe data, but lack predictive power and are thus unable to
260 build our intuition, design *de novo* input-output functions, or guide future experiments.

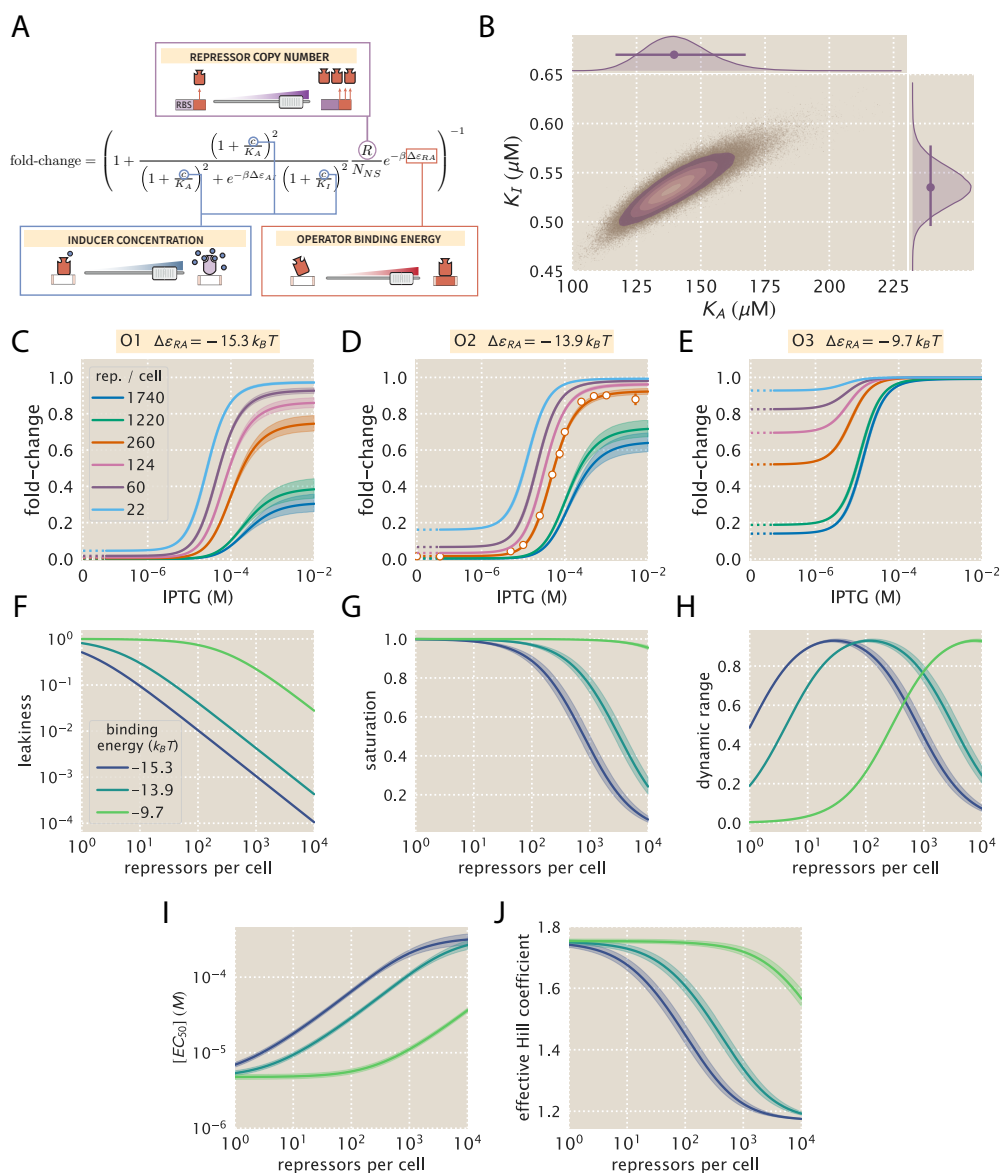


Figure 5. Predicting induction profiles for different biological control parameters. (A) We can quantitatively tune R via ribosomal binding site (RBS) modifications, $\Delta\epsilon_{RA}$ by mutating the operator sequence, and c by adding different amounts of IPTG to the growth medium. (B) Previous experiments have characterized the R , N_{NS} , $\Delta\epsilon_{RA}$, and $\Delta\epsilon_{AI}$ parameters (see Fig. 3), leaving only the unknown dissociation constants K_A and K_I between the inducer and the repressor in the active and inactive states, respectively. These two parameters can be inferred using Bayesian parameter estimation from a single induction curve. (C-E) Predicted IPTG titration curves for different repressor copy numbers and operator strengths. Titration data for the O2 strain (white circles in Panel D) with $R = 260$, $\Delta\epsilon_{RA} = -13.9 k_B T$, $n = 2$, and $\Delta\epsilon_{AI} = 4.5 k_B T$ can be used to determine the thermodynamic parameters $K_A = 139^{+29}_{-22} \times 10^{-6}$ M and $K_I = 0.53^{+0.04}_{-0.04} \times 10^{-6}$ M (orange line). The remaining solid lines predict the fold-change Eq. (5) for all other combinations of repressor copy numbers (shown in the legend) and repressor-DNA binding energies corresponding to the O1 operator ($-15.3 k_B T$), O2 operator ($-13.9 k_B T$), and O3 operator ($-9.7 k_B T$). Error bars of experimental data show the standard error of the mean (eight or more replicates) when this error is not smaller than the diameter of the data point. The shaded regions denote the 95% credible region, although the credible region is obscured when it is thinner than the curve itself. To display the measured fold-change in the absence of inducer, we alter the scaling of the x -axis between 0 and 10^{-7} M to linear rather than logarithmic, as indicated by a dashed line. Additionally, our model allows us to investigate key phenotypic properties of the induction profiles (see Fig. 1B). Specifically, we show predictions for the (F) leakiness, (G) saturation, (H) dynamic range, (I) $[EC_{50}]$, and (J) effective Hill coefficient of the induction profiles.

261 Comparison of Experimental Measurements with Theoretical Predictions

262 We tested the predictions shown in Fig. 5 by measuring the fold-change induction profiles using strains
263 that span this broad range in repressor copy numbers and repressor binding energies as characterized
264 in [14], and inducer concentrations spanning several orders of magnitude. The results, shown in Fig. 6,
265 demonstrate very good agreement between theory and experiment across all of our strains. We note,
266 however, that there was an apparently systematic shift in the O3 $\Delta\varepsilon_{RA} = -9.7 k_B T$ strains (Fig. 6C) and
267 all of the $R = 1220$ and $R = 1740$ strains. This may be partially due to imprecise previous determinations
268 of their $\Delta\varepsilon_{RA}$ and R values. By performing a global fit where we infer all parameters including the
269 repressor copy number R and the binding energy $\Delta\varepsilon_{RA}$, we found better agreement for these particular
270 strains, although a discrepancy in the steepness of the response for all O3 strains remains (see Appendix
271 F). As an additional test of our model, we also considered strains using the synthetic Oid operator which
272 exhibits stronger repression, $\Delta\varepsilon_{RA} = -17 k_B T$ [14], than the O1, O2, and O3 operators. We found that
273 we were unable to measure the strongly repressed strains accurately by flow cytometry. However, for the
274 data we collected, we found that the MWC description was consistent to within $1 k_B T$ of the binding
275 energy previously reported (see Appendix G for more details).

276 To ensure that the agreement between our predictions and data is not an accident of the strain we
277 chose to perform our fitting, we explored the effects of using each of our other strains to estimate K_A
278 and K_I . As shown in Appendix H and Fig. 6D, the inferred values of K_A and K_I depend very minimally
279 upon which strain is chosen, demonstrating that these parameter values are highly robust. As previously
280 mentioned, we performed a global fit using the data from all eighteen strains for the following parameters:
281 the inducer dissociation constants K_A and K_I , the repressor copy numbers R , and the repressor DNA
282 binding energy $\Delta\varepsilon_{RA}$ (see Appendix F). This global fit led to very similar parameter values, lending
283 strong support for our quantitative understanding of induction in the simple repression architecture. For
284 the remainder of the text we proceed using our analysis on the strain with $R = 260$ repressors and an
285 O2 operator.

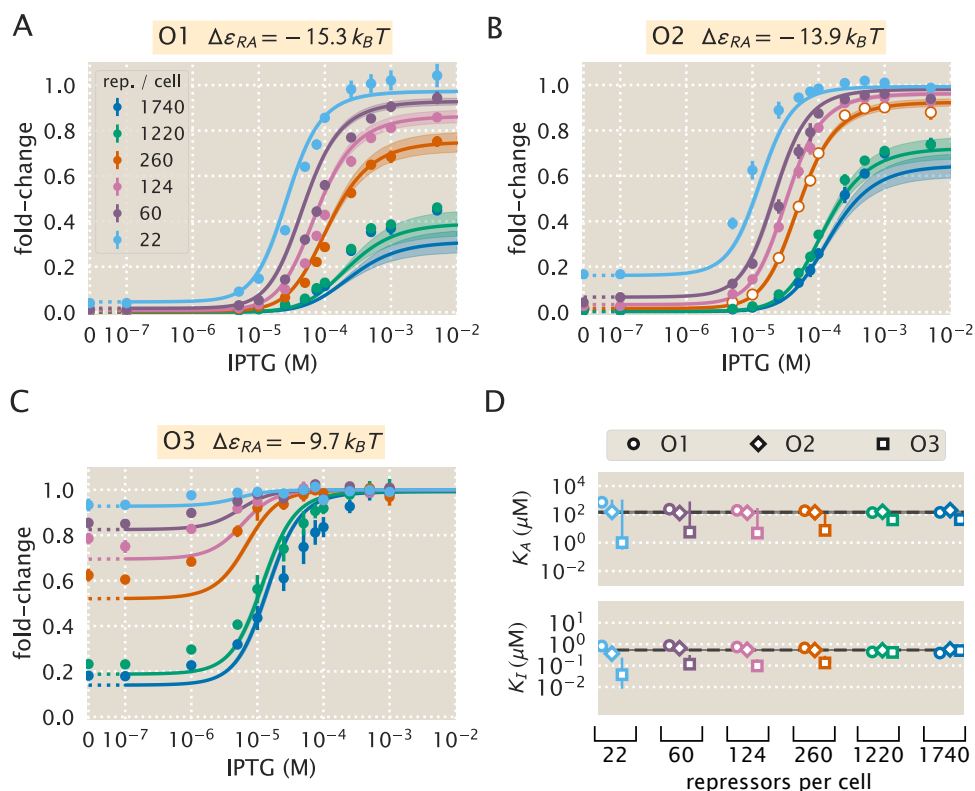


Figure 6. Comparison of predictions against measured and inferred data. Flow cytometry measurements of fold-change over a range of IPTG concentrations for (A) O1, (B) O2, and (C) O3 strains at varying repressor copy numbers, overlaid on the predicted responses. Error bars of the experimental data show the standard error of the mean (eight or more replicates). As discussed in Fig. 5, all of the predicted induction curves were created prior to measurement by inferring the MWC parameters using a single data set (O2 $R = 260$, shown by white circles in Panel B). The predictions may therefore depend upon which strain is used to infer the parameters. (D) The inferred parameter values of the dissociation constants K_A and K_I using any of the eighteen strains instead of the O2 $R = 260$ strain. Nearly identical parameter values are inferred from each strain, demonstrating that the same set of induction profiles would have been predicted regardless of which strain was chosen. The points show the mode and the error bars denote the 95% credible region of the parameter value distribution. Error bars not visible are smaller than the size of the marker.

286 Predicting the Phenotypic Traits of the Induction Response

287 Rather than measuring the full induction response of a system, a subset of the properties shown in
 288 Fig. 1, namely, the leakiness, saturation, dynamic range, $[EC_{50}]$, and effective Hill coefficient, may be
 289 of greater interest. For example, synthetic biology is often focused on generating large responses (i.e.
 290 a large dynamic range) or finding a strong binding partner (i.e. a small $[EC_{50}]$) [38, 39]. While these
 291 properties are all individually informative, when taken together they capture the essential features of the
 292 induction response. We reiterate that a Hill function approach cannot predict these features *a priori*
 293 and furthermore requires fitting each curve individually. The MWC model, on the other hand, enables
 294 us to quantify how each trait depends upon a single set of physical parameters as shown by Fig. 5F-J.

295 We define these five phenotypic traits using expressions derived from the model, Eq. (5). These
 296 results build upon extensive work by Martins and Swain, who computed many such properties for
 297 ligand-receptor binding within the MWC model [9]. We begin by analyzing the leakiness, which is the

298 minimum fold-change observed in the absence of ligand, given by

$$\begin{aligned} \text{leakiness} &= \text{fold-change}(c = 0) \\ &= \left(1 + \frac{1}{1 + e^{-\beta\Delta\varepsilon_{AI}}} \frac{R}{N_{NS}} e^{-\beta\Delta\varepsilon_{RA}} \right)^{-1}, \end{aligned} \quad (6)$$

299 and the saturation, which is the maximum fold change observed in the presence of saturating ligand,

$$\begin{aligned} \text{saturation} &= \text{fold-change}(c \rightarrow \infty) \\ &= \left(1 + \frac{1}{1 + e^{-\beta\Delta\varepsilon_{AI}}} \frac{R}{\left(\frac{K_A}{K_I}\right)^n N_{NS}} e^{-\beta\Delta\varepsilon_{RA}} \right)^{-1}. \end{aligned} \quad (7)$$

300 Systems that minimize leakiness repress strongly in the absence of effector while systems that
301 maximize saturation have high expression in the presence of effector. Together, these two properties
302 determine the dynamic range of a system's response, which is given by the difference

$$\text{dynamic range} = \text{saturation} - \text{leakiness}. \quad (8)$$

303 These three properties are shown in Fig. 5F-H. We discuss these properties in greater detail in Appendix
304 I. For example, we compute the number of repressors R necessary to evoke the maximum dynamic
305 range and demonstrate that the magnitude of this maximum is independent of the repressor-operator
306 binding energy $\Delta\varepsilon_{RA}$. Fig. 7A-C show that the measurements of these three properties, derived from
307 the fold-change data in the absence of IPTG and the presence of saturating IPTG, closely match the
308 predictions for all three operators.

309 Two additional properties of induction profiles are the $[EC_{50}]$ and effective Hill coefficient, which
310 determine the range of inducer concentration in which the system's output goes from its minimum to
311 maximum value. The $[EC_{50}]$ denotes the inducer concentration required to generate a system response
312 Eq. (5) halfway between its minimum and maximum value,

$$\text{fold-change}(c = [EC_{50}]) = \frac{\text{leakiness} + \text{saturation}}{2}. \quad (9)$$

313 The effective Hill coefficient h , which quantifies the steepness of the curve at the $[EC_{50}]$ [10], is given by

$$h = \left(2 \frac{d}{d \log c} \left[\log \left(\frac{\text{fold-change}(c) - \text{leakiness}}{\text{dynamic range}} \right) \right] \right)_{c=[EC_{50}]}. \quad (10)$$

314 Fig. 5I-J shows how the $[EC_{50}]$ and effective Hill coefficient depend on the repressor copy number. In
315 Appendix I, we discuss the analytic forms of these two properties as well as their dependence on the
316 repressor-DNA binding energy.

317 Fig. 7D-E show the estimated values of the $[EC_{50}]$ and the effective Hill coefficient overlaid on the
318 theoretical predictions. Both properties were obtained by fitting Eq. (5) to each individual titration
319 curve and computing the $[EC_{50}]$ and effective Hill coefficient using Eq. (9) and Eq. (10), respectively.
320 We find that the predictions made with the single strain fit closely match those made for each of the
321 strains with O1 and O2 operators, but the predictions for the O3 operator are markedly off. The large,
322 asymmetric error bars for the O3 $R = 22$ strain arise from its nearly flat response, where the lack of
323 dynamic range makes it impossible to determine the value of the inducer dissociation constants K_A and
324 K_I ; consequently the determination of $[EC_{50}]$ is accompanied with significant uncertainty.

325 Data Collapse of Induction Profiles

326 Our primary interest heretofore was to determine the system response at a specific inducer concentration,
327 repressor copy number, and repressor-DNA binding energy. We now flip this question on its head and

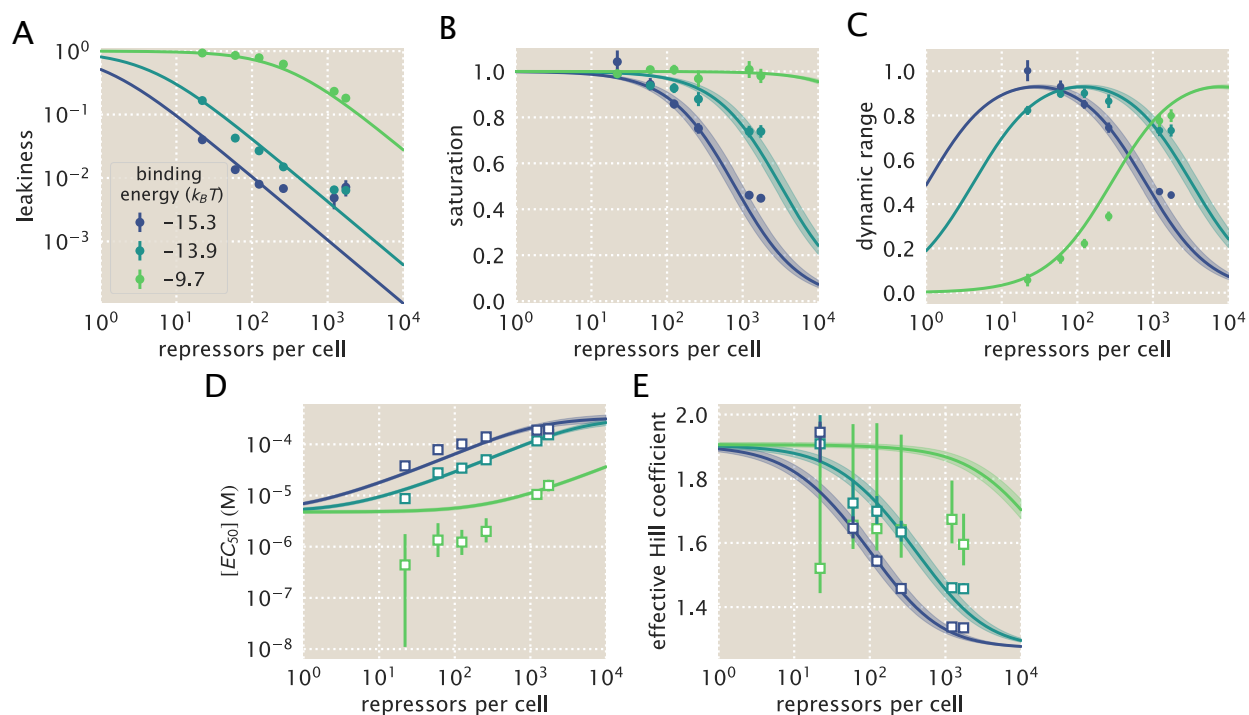


Figure 7. Predictions and experimental measurements of key properties of induction profiles. Data for the (A) leakiness, (B) saturation, and (C) dynamic range are obtained from fold-change measurements in Fig. 6 in the absence of IPTG and at saturating concentrations of IPTG. The three repressor-operator binding energies in the legend correspond to the O1 operator ($-15.3 k_B T$), O2 operator ($-13.9 k_B T$), and O3 operator ($-9.7 k_B T$). Both the (D) $[EC_{50}]$ and (E) effective Hill coefficient are inferred by individually fitting each operator-repressor pairing in Fig. 6A-C separately to Eq. (5) in order to smoothly interpolate between the data points. Error bars for A-C represent the standard error of the mean for eight or more replicates; error bars for D-E represent the 95% credible region for the parameter found by propagating the credible region of our estimates of K_A and K_I into Eqs. (9) and (10).

328 ask: given a specific value of the fold-change, what combination of parameters will give rise to this
 329 desired response? In other words, what trade-offs between the parameters of the system will give rise
 330 to the same mean cellular output? These are key questions both for understanding how the system is
 331 governed and for engineering specific responses in a synthetic biology context. To this end, we rewrite
 332 Eq. (5) as a Fermi function,

$$\text{fold-change} = \frac{1}{1 + e^{-\beta F(c)}}, \quad (11)$$

333 where $F(c)$ is the free energy of the repressor binding to the operator of interest relative to the unbound
 334 operator state [23, 24, 31], which is given by

$$F(c) = -k_B T \left(\log \frac{\left(1 + \frac{c}{K_A}\right)^n}{\left(1 + \frac{c}{K_A}\right)^n + e^{-\beta \Delta \varepsilon_{AI}} \left(1 + \frac{c}{K_I}\right)^n} + \log \frac{R}{N_{NS}} - \frac{\Delta \varepsilon_{RA}}{k_B T} \right). \quad (12)$$

335 The first term in the parenthesis denotes the contribution from the inducer concentration, the second
 336 the effect of the repressor copy number, and the last the repressor-operator binding energy. We note
 337 that elsewhere, this free energy has been dubbed the Bohr parameter since such families of curves are
 338 analogous to the shifts in hemoglobin binding curves at different pHs known as the Bohr effect [31, 40, 41].

339 Instead of analyzing each induction curve individually, the free energy provides a natural means to
340 simultaneously characterize the diversity in our eighteen induction profiles. Fig. 8A demonstrates how
341 the various induction curves from Fig. 5C-E all collapse onto a single master curve, where points from
342 every induction profile that yield the same fold-change are mapped onto the same free energy. Fig. 8B
343 shows this data collapse for the 216 data points in Fig. 6A-C, demonstrating the close match between
344 the theoretical predictions and experimental measurements across all eighteen strains.

345 There are many different combinations of parameter values that can result in the same free energy
346 as defined in Eq. (12). For example, suppose a system originally has a fold-change of 0.2 at a specific
347 inducer concentration, and then operator mutations increase the $\Delta\varepsilon_{RA}$ binding energy. While this serves
348 to initially increase both the free energy and the fold-change, a subsequent increase in the repressor copy
349 number could bring the cell back to the original fold-change level. Such trade-offs hint that there need
350 not be a single set of parameters that evoke a specific cellular response, but rather that the cell explores
351 a large but degenerate space of parameters with multiple, equally valid paths.

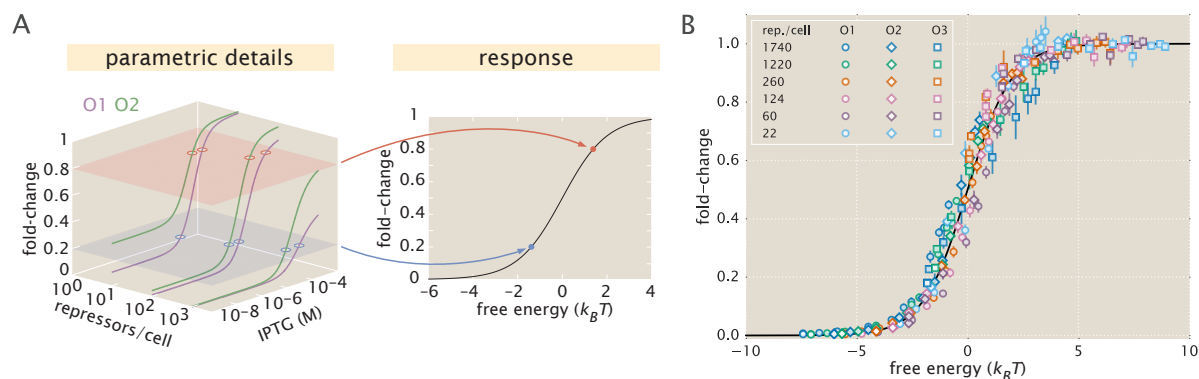


Figure 8. Fold-change data from a broad collection of different strains collapse onto a single master curve. (A) Any combination of parameters can be mapped to a single physiological response (i.e. fold-change) via the free energy, which encompasses the parametric details of the model. (B) Experimental data from Fig. 6 collapse onto a single master curve as a function of the free energy Eq. (12). The free energy for each strain was calculated from Eq. (12) using $n = 2$, $\Delta\varepsilon_{AI} = 4.5 k_B T$, $K_A = 139 \times 10^{-6} \text{ M}$, $K_I = 0.53 \times 10^{-6} \text{ M}$, and the strain specific R and $\Delta\varepsilon_{RA}$. All data points represent the mean and error bars are the standard error of the mean for eight or more replicates.

Discussion

353 Since the early work by Monod, Wyman, and Changeux [17, 42], a broad list of different biological
354 phenomena have been tied to the existence of macromolecules that switch between inactive and active
355 states. Examples can be found in a wide variety of cellular processes that include ligand-gated ion
356 channels [43], enzymatic reactions [41, 44], chemotaxis [24], quorum sensing [23], G-protein coupled
357 receptors [45], physiologically important proteins [46, 47], and beyond. One of the most ubiquitous
358 examples of allostery is in the context of gene expression, where an array of molecular players bind to
359 transcription factors to either aid or deter their ability to regulate gene activity [25, 26]. Nevertheless, no
360 definitive study has been made of the applicability of the MWC model to transcription factor function,
361 despite the clear presence of different conformational states in their structures in the presence and
362 absence of signaling molecules [48]. A central goal of this work was to assess whether a thermodynamic
363 MWC model can provide an accurate input-output function for gene regulation by allosteric transcription
364 factors.

365 Others have developed quantitative models describing different aspects of allosteric regulatory systems.
366 Martins and Swain analytically derived fundamental properties of the MWC model, including the leakiness
367 and dynamic range described in this work, noting the inherent trade-offs in these properties when tuning
368 the microscopic parameters of the model [9, 10]. Work in the Church and Voigt labs, among others, has
369 expanded on the availability of allosteric circuits for synthetic biology [7, 8, 49, 50]. Recently, Daber *et al.*
370 theoretically explored the induction of simple repression within the MWC model [3] and experimentally
371 measured how mutations alter the induction profiles of transcription factors [11]. Vilar and Saiz considered
372 the broad range of interactions in inducible *lac*-based systems including the effects of oligomerization
373 and DNA folding on transcription factor induction [6, 51]. Other work has attempted to use the *lac*
374 system to reconcile *in vitro* and *in vivo* measurements [12, 52]. Although this body of work has done
375 much to improve our understanding of allosteric transcription factors, there has remained a disconnect
376 between model and experiment. In order to rigorously test a model's applicability to natural systems,
377 the model's predictions must be weighed against data from precise experiments specifically designed to
378 test those predictions.

379 Here, we expand upon this body of work by generating a predictive model of allosteric transcriptional
380 regulation and then testing the model against a thorough set of experiments using well-characterized
381 regulatory components. Specifically, we used the MWC model to build upon and refine a well-established
382 thermodynamic model of transcriptional regulation [14, 18], allowing us to compose the model from
383 a minimal set of biologically meaningful parameters. This minimal model captures the key players
384 of transcriptional regulation – namely the repressor copy number, the DNA binding energy, and the
385 concentration of inducer – and enables us to predict how the system will behave when we change each
386 of these parameters. We tested these predictions on a range of strains whose repressor copy number
387 spanned two orders of magnitude and whose DNA binding affinity spanned $6 k_B T$. We argue that one
388 would not be able to generate such a wide array of predictions by using a Hill function, which abstracts
389 away the biophysical meaning of the parameters into phenomenological parameters [53].

390 Specifically, we tested our model in the context of a *lac*-based simple repression system by first
391 determining the allosteric dissociation constants K_A and K_I from a single induction data set (O2 operator
392 with binding energy $\Delta\epsilon_{RA} = -13.9 k_B T$ and repressor copy number $R = 260$) and then using these
393 values to make parameter-free predictions of the induction profiles for seventeen other strains where $\Delta\epsilon_{RA}$
394 and R were varied significantly (see Fig. 5). We next measured the induction profiles of these seventeen
395 strains using flow cytometry and found that our predictions consistently and accurately captured the
396 primary features for each induction data set, as shown in Fig. 6A-C. Surprisingly, we find that the
397 inferences for the repressor-inducer dissociation constants that would have been derived from any other
398 single strain (instead of the O2 operator with $R = 260$) would have resulted in nearly identical predictions
399 (see Fig. 6D and Appendix H). This suggests that a few carefully chosen measurements can lead to a
400 deep quantitative understanding of how simple regulatory systems work without requiring an extensive
401 sampling of strains that span the parameter space. Moreover, the fact that we could consistently achieve
402 reliable predictions after fitting only two free parameters stands in contrast to the common practice of
403 fitting several free parameters simultaneously, which can nearly guarantee an acceptable fit provided

404 that the model roughly resembles the system response, regardless of whether the details of the model are
405 tied to any underlying molecular mechanism.

406 Beyond observing changes in fold-change as a function of effector concentration, our application of the
407 MWC model allows us to explicitly predict the values of the induction curves' key parameters, namely,
408 the leakiness, saturation, dynamic range, $[EC_{50}]$, and the effective Hill coefficient (see Fig. 7). This
409 allows us to quantify the unique traits of each set of strains examined here. Strains using the O1 operator
410 consistently have a low leakiness value, a consequence of its strong binding energy. The saturation values
411 for these strains, however, vary significantly with R . This trend is reversed for strains using O3, which
412 has the weakest binding energy of our constructs. Leakiness values for constructs using O3 vary strongly
413 with R , but their saturation values approach 1 regardless of R . Strains with the intermediate O2 binding
414 energy have both a leakiness and saturation that vary markedly with R . For both the O1 and O2 data
415 sets, our model also accurately predicts the effective Hill coefficient and $[EC_{50}]$, though these predictions
416 for O3 are noticeably less accurate. While performing a global fit for all model parameters marginally
417 improves the prediction for O3 (see Appendix F), we are still unable to accurately predict the effective
418 Hill coefficient or the $[EC_{50}]$, though the uncertainties in these two parameters are really an inheritance
419 from the consistent difference between the theoretical and measured sharpness of the induction response
420 seen in Fig. 6C.

421 Because this model allows us to derive expressions for individual features of induction curves, we are
422 able to examine how these features may be tuned by careful selection of system parameters. Fig. 7 shows
423 how each of the induction curves' key features vary as a function of $\Delta\varepsilon_{RA}$ and R , which makes it possible
424 to select desired properties from among the possible phenotypes available to the system. For instance, it
425 is possible to obtain a high dynamic range using fewer than 100 repressors if the binding energy is strong.
426 As an example of the constraints inherent to the system, one cannot design a strain with a leakiness of
427 0.1 and a saturation of 0.4 by only varying the repressor copy number and repressor-operator binding
428 affinity, since these two properties are coupled by Eqs. (6) and (7). Achieving this particular behavior
429 would require changing the ratio K_A/K_I of repressor-inducer dissociation constants, as may be done by
430 mutating the repressor's inducer binding pocket.

431 The dynamic range, which is of considerable interest when designing or characterizing a genetic
432 circuit, is revealed to have an interesting property: although changing the value of $\Delta\varepsilon_{RA}$ causes the
433 dynamic range curves to shift to the right or left, each curve has the same shape and in particular the
434 same maximum value. This means that strains with strong or weak binding energies can attain the
435 same dynamic range when the value of R is tuned to compensate for this energy. This feature is not
436 immediately apparent from the IPTG induction curves, which show very low dynamic ranges for several
437 of the O1 and O3 strains. Without the benefit of models that can predict such phenotypic traits, efforts
438 to engineer genetic circuits with allosteric transcription factors must rely on trial and error to achieve
439 specific responses [7, 8]. This is a compelling example showing that our predictive modeling approach
440 has a significant advantage over descriptive models.

441 To our knowledge this is the first work of its kind in which a single family of parameters is demonstrated
442 to predict a vast range of induction curves with qualitatively different behaviors. One of the demanding
443 criteria of our approach is that a small set of parameters must consistently describe data from a diverse
444 collection of data sets taken using distinct methods such as Miller assays and bulk and single-cell
445 fluorescence experiments to measure fold-change (see Appendices C and G), as well as quantitative
446 Western blots [14] and binomial partitioning methods to count repressors [15, 54]. Furthermore, we build
447 off of our previous studies that use the simple repression architecture and we demand that the parameters
448 derived from these studies account for constructs that are integrated into the chromosome, plasmid-borne,
449 and even for cases where there are competing binding sites to take repressors out of circulation [14, 15]
450 (see Appendix B) or where there are multiple operators to allow DNA looping [21]. The resulting model
451 not only predicts the individual titration profiles as a function of IPTG, but describes key properties of
452 the response. The general agreement with the entire body of work presented here demonstrates that
453 our model captures the underlying mechanism governing simple repression. We are unaware of any
454 comparable study in transcriptional regulation that demands one predictive framework cover such a
455 broad array of regulatory situations.

456 Despite the diversity observed in the induction profiles of each of our strains, our data are unified by
457 their reliance on fundamental biophysical parameters. In particular, we have shown that our model for
458 fold-change can be rewritten in terms of the free energy Eq. (12), which encompasses all of the physical
459 parameters of the system. This has proven to be an illuminating technique in a number of studies of
460 allosteric proteins [23, 24, 55]. Although it is experimentally straightforward to observe system responses
461 to changes in effector concentration c , framing the input-output function in terms of c can give the
462 misleading impression that changes in system parameters lead to fundamentally altered system responses.
463 Alternatively, if one can find the “natural variable” that enables the output to collapse onto a single
464 curve, it becomes clear that the system’s output is not governed by individual system parameters, but
465 rather the contributions of multiple parameters that define the natural variable.

466 When our fold-change data are plotted against the respective free energies for each construct, they
467 collapse cleanly onto a single curve (see Fig. 8). This enables us to analyze how parameters can
468 compensate each other. For example, we may wish to determine which combinations of parameters result
469 in a system that is strongly repressed (free energy $F(c) \leq -5 k_B T$). We know from our understanding
470 of the induction phenomenon that strong repression is most likely to occur at low values of c . However,
471 from Eq. (12) we can clearly see that increases in the value of c can be compensated by an increase in
472 the number of repressors R , a decrease in the binding energy $\Delta\varepsilon_{RA}$ (i.e. stronger binding), or some
473 combination of both. Likewise, while the system tends to express strongly ($F(c) \geq 5 k_B T$) when c is
474 high, one could design a system that expresses strongly at low values of c by reducing R or increasing
475 the value of $\Delta\varepsilon_{RA}$. As a concrete example, given a concentration $c = 10^{-5}$ M, a system using the O1
476 operator ($\Delta\varepsilon_{RA} = -15.3 k_B T$) requires 745 or more repressors for $F(c) \leq -5 k_B T$, while a system using
477 the weaker O3 operator ($\Delta\varepsilon_{RA} = -9.7 k_B T$) requires 2×10^5 or more repressors for $F(c) \leq -5 k_B T$.

478 While our experiments validated the theoretical predictions in the case of simple repression, we expect
479 the framework presented here to apply much more generally to different biological instances of allosteric
480 regulation. For example, we can use this model to explore different regulatory configurations such as
481 corepression, activation, and coactivation, each of which are found in *E. coli* (see Appendix J). This work
482 can also serve as a springboard to characterize not just the mean but the full gene expression distribution
483 and thus quantify the impact of noise on this system [56]. Another extension of this approach would be
484 to theoretically predict and experimentally verify whether the repressor-inducer dissociation constants
485 K_A and K_I or the energy difference $\Delta\varepsilon_{AI}$ between the allosteric states can be tuned by making single
486 amino acid substitutions in the transcription factor [11, 31]. Finally, we expect that the kind of rigorous
487 quantitative description of the allosteric phenomenon provided here will make it possible to construct
488 biophysical models of fitness for allosteric proteins similar to those already invoked to explore the fitness
489 effects of transcription factor binding site strengths and protein stability [57–59].

490 To conclude, we find that our application of the MWC model provides an accurate, predictive
491 framework for understanding simple repression by allosteric transcription factors. To reach this conclusion,
492 we analyzed the model in the context of a well-characterized system, in which each parameter had a clear
493 biophysical meaning. As many of these parameters had been measured or inferred in previous studies,
494 this gave us a minimal model with only two free parameters which we inferred from a single data set.
495 We then accurately predicted the behavior of seventeen other data sets in which repressor copy number
496 and repressor-DNA binding energy were systematically varied. In addition, our model allowed us to
497 understand how key properties such as the leakiness, saturation, dynamic range, $[EC_{50}]$, and effective
498 Hill coefficient depended upon the small set of parameters governing this system. Finally, we show that
499 by framing inducible simple repression in terms of free energy, the data from all of our experimental
500 strains collapse cleanly onto a single curve, illustrating the many ways in which a particular output
501 can be targeted. In total, these results show that a thermodynamic formulation of the MWC model
502 supersedes phenomenological fitting functions for understanding transcriptional regulation by allosteric
503 proteins.

504 Methods

505 Bacterial Strains and DNA Constructs

506 All strains used in these experiments were derived from *E. coli* K12 MG1655 with the *lac* operon removed,
507 adapted from those created and described in [14, 19]. Briefly, the operator variants and YFP reporter
508 gene were cloned into a pZS25 background which contains a *lacUV5* promoter that drives expression
509 as is shown in Fig. 2. These constructs carried a kanamycin resistance gene and were integrated into
510 the *galK* locus of the chromosome using λ Red recombineering [60]. The *lacI* gene was constitutively
511 expressed via a $P_{LtetO-1}$ promoter [50], with ribosomal binding site mutations made to vary the LacI copy
512 number as described in [61] using site-directed mutagenesis (Quickchange II; Stratagene), with further
513 details in [14]. These *lacI* constructs carried a chloramphenicol resistance gene and were integrated into
514 the *ybcN* locus of the chromosome. Final strain construction was achieved by performing repeated P1
515 transduction [62] of the different operator and *lacI* constructs to generate each combination used in
516 this work. Integration was confirmed by PCR amplification of the replaced chromosomal region and by
517 sequencing. Primers and final strain genotypes are listed in Appendix K.

518 It is important to note that the rest of the *lac* operon (*lacZYA*) was never expressed. The LacY
519 protein is a transmembrane protein which actively transports lactose as well as IPTG into the cell.
520 As LacY was never produced in our strains, we assume that the extracellular and intracellular IPTG
521 concentration was approximately equal due to diffusion across the membrane into the cell as is suggested
522 by previous work [63].

523 To make this theory applicable to transcription factors with any number of DNA binding domains,
524 we used a different definition for repressor copy number than has been used previously. We define the
525 LacI copy number as the average number of repressor dimers per cell whereas in [14], the copy number is
526 defined as the average number of repressor tetramers in each cell. To motivate this decision, we consider
527 the fact that the LacI repressor molecule exists as a tetramer in *E. coli* [48] in which a single DNA
528 binding domain is formed from dimerization of LacI proteins, so that wild-type LacI might be described
529 as dimer of dimers. Since each dimer is allosterically independent (i.e. either dimer can be allosterically
530 active or inactive, independent of the configuration of the other dimer) [3], a single LacI tetramer can
531 be treated as two functional repressors. Therefore, we have simply multiplied the number of repressors
532 reported in [14] by a factor of two. This factor is included as a keyword argument in the numerous
533 Python functions used to perform this analysis, as discussed in the code documentation.

534 A subset of strains in these experiments were measured using fluorescence microscopy for validation
535 of the flow cytometry data and results. To aid in the high-fidelity segmentation of individual cells, the
536 strains were modified to constitutively express an mCherry fluorophore. This reporter was cloned into a
537 pZS4*1 backbone [50] in which mCherry is driven by the *lacUV5* promoter. All microscopy and flow
538 cytometry experiments were performed using these strains.

539 Growth Conditions for Flow Cytometry Measurements

540 All measurements were performed with *E. coli* cells grown to mid-exponential phase in standard M9
541 minimal media (M9 5X Salts, Sigma-Aldrich M6030; 2 mM magnesium sulfate, Mallinckrodt Chemicals
542 6066-04; 100 μ M calcium chloride, Fisher Chemicals C79-500) supplemented with 0.5% (w/v) glucose.
543 Briefly, 500 μ L cultures of *E. coli* were inoculated into Lysogeny Broth (LB Miller Powder, BD Medical)
544 from a 50% glycerol frozen stock (-80° C) and were grown overnight in a 2 mL 96-deep-well plate sealed
545 with a breathable nylon cover (Lab Pak - Nitex Nylon, Sefar America Inc. Cat. No. 241205) with
546 rapid agitation for proper aeration. After approximately 12 to 15 hours, the cultures had reached
547 saturation and were diluted 1000-fold into a second 2 mL 96-deep-well plate where each well contained
548 500 μ L of M9 minimal media supplemented with 0.5% w/v glucose (anhydrous D-Glucose, Macron
549 Chemicals) and the appropriate concentration of IPTG (Isopropyl β -D-1 thiogalactopyranoside Dioxane
550 Free, Research Products International). These were sealed with a breathable cover and were allowed to
551 grow for approximately eight hours. Cells were then diluted ten-fold into a round-bottom 96-well plate
552 (Corning Cat. No. 3365) containing 90 μ L of M9 minimal media supplemented with 0.5% w/v glucose

553 along with the corresponding IPTG concentrations. For each IPTG concentration, a stock of 100-fold
554 concentrated IPTG in double distilled water was prepared and partitioned into 100 μ L aliquots. The
555 same parent stock was used for all experiments described in this work.

556 Flow Cytometry

557 Unless explicitly mentioned, all fold-change measurements were collected on a Miltenyi Biotec MACSQuant
558 Analyzer 10 Flow Cytometer graciously provided by the Pamela Björkman lab at Caltech. Detailed
559 information regarding the voltage settings of the photo-multiplier detectors can be found in Appendix
560 Table S1. Prior to each day’s experiments, the analyzer was calibrated using MACSQuant Calibration
561 Beads (Cat. No. 130-093-607) such that day-to-day experiments would be comparable. All YFP
562 fluorescence measurements were collected via 488 nm laser excitation coupled with a 525/50 nm emission
563 filter. Unless otherwise specified, all measurements were taken over the course of two to three hours
564 using automated sampling from a 96-well plate kept at approximately 4° - 10°C on a MACS Chill 96
565 Rack (Cat. No. 130-094-459). Cells were diluted to a final concentration of approximately 4×10^4 cells
566 per μ L which corresponded to a flow rate of 2,000-6,000 measurements per second, and acquisition for
567 each well was halted after 100,000 events were detected. Once completed, the data were extracted and
568 immediately processed using the following methods.

569 Unsupervised Gating of Flow Cytometry Data

570 Flow cytometry data will frequently include a number of spurious events or other undesirable data
571 points such as cell doublets and debris. The process of restricting the collected data set to those data
572 determined to be “real” is commonly referred to as gating. These gates are typically drawn manually [64]
573 and restrict the data set to those points which display a high degree of linear correlation between their
574 forward-scatter (FSC) and side-scatter (SSC). The development of unbiased and unsupervised methods
575 of drawing these gates is an active area of research [65, 66]. For our purposes, we assume that the
576 fluorescence level of the population should be log-normally distributed about some mean value. With
577 this assumption in place, we developed a method that allows us to restrict the data used to compute the
578 mean fluorescence intensity of the population to the smallest two-dimensional region of the log(FSC) vs.
579 log(SSC) space in which 40% of the data is found. This was performed by fitting a bivariate Gaussian
580 distribution and restricting the data used for calculation to those that reside within the 40th percentile.
581 This procedure is described in more detail in the supplementary information as well as in a Jupyter
582 notebook located in this paper’s [Github repository](#).

583 Experimental Determination of Fold-Change

584 For each strain and IPTG concentration, the fold-change in gene expression was calculated by taking
585 the ratio of the population mean YFP expression in the presence of LacI repressor to that of the
586 population mean in the absence of LacI repressor. However, the measured fluorescence intensity of each
587 cell also includes the autofluorescence contributed by the weak excitation of the myriad protein and
588 small molecules within the cell. To correct for this background, we computed the fold change as

$$\text{fold-change} = \frac{\langle I_{R>0} \rangle - \langle I_{\text{auto}} \rangle}{\langle I_{R=0} \rangle - \langle I_{\text{auto}} \rangle}, \quad (13)$$

589 where $\langle I_{R>0} \rangle$ is the average cell YFP intensity in the presence of repressor, $\langle I_{R=0} \rangle$ is the average cell
590 YFP intensity in the absence of repressor, and $\langle I_{\text{auto}} \rangle$ is the average cell autofluorescence intensity, as
591 measured from cells that lack the *lac*-YFP construct.

592 Bayesian Parameter Estimation

593 In this work, we determine the the most-likely parameter values for the inducer dissociation constants
594 K_A and K_I of the active and inactive state, respectively, using Bayesian methods. We compute the

595 probability distribution of the value of each parameter given the data D , which by Bayes' theorem is
 596 given by

$$P(K_A, K_I | D) = \frac{P(D | K_A, K_I)P(K_A, K_I)}{P(D)}, \quad (14)$$

597 where D is all the data composed of independent variables (repressor copy number R , repressor-DNA
 598 binding energy $\Delta\varepsilon_{RA}$, and inducer concentration c) and one dependent variable (experimental fold-
 599 change). $P(D | K_A, K_I)$ is the likelihood of having observed the data given the parameter values for
 600 the dissociation constants, $P(K_A, K_I)$ contains all the prior information on these parameters, and $P(D)$
 601 serves as a normalization constant, which we can ignore in our parameter estimation. Eq. (5) assumes a
 602 deterministic relationship between the parameters and the data, so in order to construct a probabilistic
 603 relationship as required by Eq. (14), we assume that the experimental fold-change for the i^{th} datum
 604 given the parameters is of the form

$$\text{fold-change}_{\text{exp}}^{(i)} = \left(1 + \frac{\left(1 + \frac{c^{(i)}}{K_A}\right)^2}{\left(1 + \frac{c^{(i)}}{K_A}\right)^2 + e^{-\beta\Delta\varepsilon_{AI}} \left(1 + \frac{c^{(i)}}{K_I}\right)^2} \frac{R^{(i)}}{N_{NS}} e^{-\beta\Delta\varepsilon_{RA}^{(i)}} \right)^{-1} + \epsilon^{(i)}, \quad (15)$$

605 where $\epsilon^{(i)}$ represents the departure from the deterministic theoretical prediction for the i^{th} data point. If
 606 we assume that these $\epsilon^{(i)}$ errors are normally distributed with mean zero and standard deviation σ , the
 607 likelihood of the data given the parameters is of the form

$$P(D|K_A, K_I, \sigma) = \frac{1}{(2\pi\sigma^2)^{\frac{n}{2}}} \prod_{i=1}^n \exp \left[-\frac{(\text{fold-change}_{\text{exp}}^{(i)} - \text{fold-change}(K_A, K_I, R^{(i)}, \Delta\varepsilon_{RA}^{(i)}, c^{(i)}))^2}{2\sigma^2} \right], \quad (16)$$

608 where $\text{fold-change}_{\text{exp}}^{(i)}$ is the experimental fold-change and $\text{fold-change}(\dots)$ is the theoretical prediction.
 609 The product $\prod_{i=1}^n$ captures the assumption that the n data points are independent. Note that the
 610 likelihood and prior terms now include the extra unknown parameter σ . In applying Eq. (16), a choice of
 611 K_A and K_I that provides better agreement between theoretical fold-change predictions and experimental
 612 measurements will result in a more probable likelihood.

613 Both mathematically and numerically, it is convenient to define $\tilde{k}_A = -\log \frac{K_A}{1\text{M}}$ and $\tilde{k}_I = -\log \frac{K_I}{1\text{M}}$
 614 and fit for these parameters on a log scale. Dissociation constants are scale invariant, so that a change
 615 from $10\ \mu\text{M}$ to $1\ \mu\text{M}$ leads to an equivalent increase in affinity as a change from $1\ \mu\text{M}$ to $0.1\ \mu\text{M}$. With
 616 these definitions we assume for the prior $P(\tilde{k}_A, \tilde{k}_I, \sigma)$ that all three parameters are independent. In
 617 addition, we assume a uniform distribution for \tilde{k}_A and \tilde{k}_I and a Jeffreys prior [36] for the scale parameter
 618 σ . This yields the complete prior

$$P(\tilde{k}_A, \tilde{k}_I, \sigma) \equiv \frac{1}{(\tilde{k}_A^{\text{max}} - \tilde{k}_A^{\text{min}})} \frac{1}{(\tilde{k}_I^{\text{max}} - \tilde{k}_I^{\text{min}})} \frac{1}{\sigma}. \quad (17)$$

619 These priors are maximally uninformative meaning that they imply no prior knowledge of the parameter
 620 values. We defined the \tilde{k}_A and \tilde{k}_I ranges uniform on the range of -7 to 7 , although we note that this
 621 particular choice does not affect the outcome provided the chosen range is sufficiently wide.

622 Putting all these terms together we can now sample from $P(\tilde{k}_A, \tilde{k}_I, \sigma | D)$ using Markov chain Monte
 623 Carlo (see [GitHub repository](#)) to compute the most likely parameter as well as the error bars (given by
 624 the 95% credible region) for K_A and K_I .

625 Data Curation

626 All of the data used in this work as well as all relevant code can be found at this [dedicated website](#). Data
 627 were collected, stored, and preserved using the Git version control software in combination with off-site
 628 storage and hosting website GitHub. Code used to generate all figures and complete all processing step
 629 as and analyses are available on the GitHub repository. Many analysis files are stored as instructive
 630 Jupyter Notebooks. The scientific community is invited to fork our repositories and open constructive
 631 issues on the [GitHub repository](#).

632 **Acknowledgements**

633 This work has been a wonderful exercise in scientific collaboration. We thank Hernan Garcia for
634 information and advice for working with these bacterial strains, Pamela Björkman and Rachel Galimidi
635 for access and training for use of the Miltenyi Biotec MACSQuant flow cytometer, and Colin deBakker
636 of Miltenyi Biotec for useful advice and instruction in flow cytometry. The experimental front of this
637 work began at the Physiology summer course at the Marine Biological Laboratory in Woods Hole, MA
638 operated by the University of Chicago. We thank Simon Alamos, Nalin Ratnayeke, and Shane McNally
639 for their work on the project during the course. We also thank Suzannah Beeler, Justin Bois, Robert
640 Brewster, Ido Golding, Soichi Hirokawa, Jané Kondev, Tom Kuhlman, Heun Jin Lee, Muir Morrison,
641 Nigel Orme, Alvaro Sanchez, and Julie Theriot for useful advice and discussion. We are also grateful to
642 the three anonymous reviewers for substantially improving the quality of our work and our paper. This
643 work was supported by La Fondation Pierre-Gilles de Gennes, the Rosen Center at Caltech, and the
644 National Institutes of Health DP1 OD000217 (Director's Pioneer Award), R01 GM085286, and 1R35
645 GM118043-01 (MIRA). Nathan Belliveau is a Howard Hughes Medical Institute International Student
646 Research fellow.

647 **Competing interests**

648 The authors have declared that no competing interests exist.

649 **Author contributions**

650 MRM, SB, NB, GC, and TE contributed equally to this work. MRM, SB, NB, GC performed experiments.
651 TE and MRM laid groundwork for the model. MRM, SB, NB, GC, and TE performed the data analysis.
652 MRM, GC, NB, and SB wrote code used for all experimental analysis and parameter estimation. GC
653 made the figures for the main text and GC, MRM, SB, and NB made figures for the supplemental
654 information. MRM, SB, NB, GC, TE, and RP wrote the paper. ML and RP provided useful insight and
655 advice in designing and executing the work.

References

- 656 1. Lindsley JE, Rutter J. 2006. Whence cometh the allosterome? *Proceedings of the National Academy of Sciences of USA* **103**: 10533–5.
- 657 2. Kuhlman T, Zhang Z, Saier MH, Hwa T. 2007. Combinatorial transcriptional control of the lactose
658 operon of *Escherichia coli*. *Proceedings of the National Academy of Sciences of USA* **104**: 6043–8.
- 659 3. Daber R, Sharp K, Lewis M. 2009. One is not enough. *Journal of Molecular Biology* **392**:
660 1133–1144.
- 661 4. Setty Y, Mayo AE, Surette MG, Alon U. 2003. Detailed map of a cis-regulatory input function.
662 *Proceedings of the National Academy of Sciences* **100**: 7702–7707.
- 663 5. Poelwijk F, deVos M, Tans S. 2011. Tradeoffs and optimality in the evolution of gene regulation.
664 *Cell* **146**: 462–470.
- 665 6. Vilar JMG, Saiz L. 2013. Reliable prediction of complex phenotypes from a modular design in free
666 energy space: an extensive exploration of the *lac* operon. *ACS Synthetic Biology* **2**: 576–586.
- 667 7. Rogers JK, Guzman CD, Taylor ND, Raman S, Anderson K, Church GM. 2015. Synthetic biosensors
668 for precise gene control and real-time monitoring of metabolites. *Nucleic Acids Research* **43**:
669 7648–7659.
- 670 8. Rohlhill J, Sandoval NR, Papoutsakis ET. 2017. Sort-seq approach to engineering a formaldehyde-
671 inducible promoter for dynamically regulated *Escherichia coli* growth on methanol. *ACS Synthetic
672 Biology*: Advance online publication.
- 673 9. Martins BMC, Swain PS. 2011. Trade-offs and constraints in allosteric sensing. *PLoS Computational
674 Biology* **7**: 1–13.
- 675 10. Marzen S, Garcia HG, Phillips R. 2013. Statistical mechanics of Monod-Wyman-Changeux (MWC)
676 models. *Journal of Molecular Biology* **425**: 1433–1460.
- 677 11. Daber R, Sochor MA, Lewis M. 2011. Thermodynamic analysis of mutant *lac* repressors. *Journal
678 of Molecular Biology* **409**: 76–87.
- 679 12. Sochor MA. 2014. *In vitro* transcription accurately predicts *lac* repressor phenotype *in vivo* in
680 *Escherichia coli*. *PeerJ* **2**: e498.
- 681 13. Rydenfelt M, Garcia HG, Cox RS, Phillips R. 2014. The influence of promoter architectures and
682 regulatory motifs on gene expression in *Escherichia coli*. *PLoS ONE* **9**: 1–31.
- 683 14. Garcia HG, Phillips R. 2011. Quantitative dissection of the simple repression input-output function.
684 *Proceedings of the National Academy of Sciences of USA* **108**: 12173–8.
- 685 15. Brewster RC, Weinert FM, Garcia HG, Song D, Rydenfelt M, Phillips R. 2014. The transcription
686 factor titration effect dictates level of gene expression. *Cell* **156**: 1312–1323.
- 687 16. Weinert FM, Brewster RC, Rydenfelt M, Phillips R, Kegel WK. 2014. Scaling of gene expression
688 with transcription-factor fugacity. *Physical Review Letters* **113**: 1–5.
- 689 17. Monod J, Wyman J, Changeux JP. 1965. On the nature of allosteric transitions: a plausible model.
690 *Journal of molecular biology* **12**: 88–118.
- 691 18. Bintu L, Buchler NE, Garcia HG, Gerland U, Hwa T, Kondev J, Phillips R. 2005. Transcriptional
692 regulation by the numbers: models. *Current Opinion in Genetics & Development* **15**: 116–124.

- 695 19. Garcia HG, Lee HJ, Boedicker JQ, Phillips R. 2011. Comparison and calibration of different
696 reporters for quantitative analysis of gene expression. *Biophysical Journal* **101**: 535–544.
- 697 20. Brewster RC, Jones DL, Phillips R. 2012. Tuning promoter strength through RNA polymerase
698 binding site design in *Escherichia coli*. *PLoS Computational Biology* **8**.
- 699 21. Boedicker JQ, Garcia HG, Phillips R. 2013. Theoretical and experimental dissection of DNA
700 loop-mediated repression. *Physical Review Letters* **110**: 018101.
- 701 22. Boedicker JQ, Garcia HG, Johnson S, Phillips R. 2013. DNA sequence-dependent mechanics and
702 protein-assisted bending in repressor-mediated loop formation. *Physical Biology* **10**: 066005.
- 703 23. Swem LR, Swem DL, Wingreen NS, Bassler BL. 2008. Deducing receptor signaling parameters
704 from *in vivo* analysis: LuxN/AI-1 quorum sensing in *Vibrio harveyi*. *Cell* **134**: 461–473.
- 705 24. Keymer JE, Endres RG, Skoge M, Meir Y, Wingreen NS. 2006. Chemosensing in *Escherichia coli*:
706 two regimes of two-state receptors. *Proceedings of the National Academy of Sciences of USA* **103**:
707 1786–91.
- 708 25. Huang Z, Zhu L, Cao Y, Wu G, Liu X, Chen Y, Wang Q, Shi T, Zhao Y, Wang Y, et al.. 2011.
709 Asd: a comprehensive database of allosteric proteins and modulators. *Nucleic Acids Research* **39**:
710 D663.
- 711 26. Li GW, Burkhardt D, Gross C, Weissman JS. 2014. Quantifying absolute protein synthesis rates
712 reveals principles underlying allocation of cellular resources. *Cell* **157**: 624–635.
- 713 27. Ackers GK, Johnson AD, Shea MA. 1982. Quantitative model for gene regulation by lambda
714 phage repressor. *Proceedings of the National Academy of Sciences of USA* **79**: 1129–33.
- 715 28. Buchler NE, Gerland U, Hwa T. 2003. On schemes of combinatorial transcription logic. *PNAS*
716 **100**: 5136–41.
- 717 29. Vilar JM, Leibler S. 2003. DNA looping and physical constraints on transcription regulation.
718 *Journal of Molecular Biology* **331**: 981–989.
- 719 30. Bintu L, Buchler NE, Garcia HG, Gerland U, Hwa T, Kondev J, Kuhlman T, Phillips R. 2005. Tran-
720 scriptional regulation by the numbers: applications. *Current Opinion in Genetics & Development*
721 **15**: 125–135.
- 722 31. Phillips R. 2015. Napoleon is in equilibrium. *Annual Review of Condensed Matter Physics* **6**:
723 85–111.
- 724 32. Klumpp S, Hwa T. 2008. Growth-rate-dependent partitioning of RNA polymerases in bacteria.
725 *Proceedings of the National Academy of Sciences of USA* **105**: 20245–50.
- 726 33. O’Gorman RB, Rosenberg JM, Kallai OB, Dickerson RE, Itakura K, Riggs AD, Matthews KS.
727 1980. Equilibrium binding of inducer to *lac* repressor-operator DNA complex. *Journal of Biological*
728 *Chemistry* **255**: 10107–10114.
- 729 34. Rydenfelt M, Cox RS, Garcia H, Phillips R. 2014. Statistical mechanical model of coupled
730 transcription from multiple promoters due to transcription factor titration. *Phys Rev E* **89**:
731 012702.
- 732 35. Oehler S, Amouyal M, Kolkhof P, von Wilcken-Bergmann B, Müller-Hill B. 1994. Quality and
733 position of the three *lac* operators of *E. coli* define efficiency of repression. *The EMBO journal*
734 **13**: 3348–3355.
- 735 36. Sivia D, Skilling J. 2006. Data analysis: a Bayesian tutorial. OUP Oxford.

- 736 37. Scott M, Gunderson CW, Mateescu EM, Zhang Z, Hwa T. 2010. Interdependence of cell growth
737 and gene expression: origins and consequences. *Science* **330**: 1099–102.
- 738 38. Brophy JAN, Voigt CA. 2014. Principles of genetic circuit design. *Nature Methods* **11**: 508–520.
- 739 39. Shis DL, Hussain F, Meinhardt S, Swint-Kruse L, Bennett MR. 2014. Modular, multi-input
740 transcriptional logic gating with orthogonal LacI/GalR family chimeras. *ACS Synthetic Biology* **3**:
741 645–651.
- 742 40. Mirny LA. 2010. Nucleosome-mediated cooperativity between transcription factors. *Proceedings of*
743 *the National Academy of Sciences of USA* **107**: 22534–9.
- 744 41. Einav T, Mazutis L, Phillips R. 2016. Statistical mechanics of allosteric enzymes. *The Journal of*
745 *Physical Chemistry B* .
- 746 42. Monod J, Changeux JP, Jacob F. 1963. Allosteric proteins and cellular control systems. *Journal*
747 *of molecular biology* **6**: 306–329.
- 748 43. Auerbach A. 2012. Thinking in cycles: MWC is a good model for acetylcholine receptor-channels.
749 *The Journal of Physiology* **590**: 93–8.
- 750 44. Velyvis A, Yang YR, Schachman HK, Kay LE. 2007. A solution NMR study showing that active site
751 ligands and nucleotides directly perturb the allosteric equilibrium in aspartate transcarbamoylase.
752 *Proceedings of the National Academy of Sciences of USA* **104**: 8815–20.
- 753 45. Canals M, Lane JR, Wen A, Scammells PJ, Sexton PM, Christopoulos A. 2012. A Monod-Wyman-
754 Changeux mechanism can explain G protein-coupled receptor (GPCR) allosteric modulation.
755 *Journal of Biological Chemistry* **287**: 650–659.
- 756 46. Levantino M, Spilotros A, Cammarata M, Schirò G, Ardiccioni C, Vallone B, Brunori M, Cupane
757 A. 2012. The Monod-Wyman-Changeux allosteric model accounts for the quaternary transition
758 dynamics in wild type and a recombinant mutant human hemoglobin. *Proceedings of the National*
759 *Academy of Sciences of USA* **109**: 14894–9.
- 760 47. Milo R, Hou JH, Springer M, Brenner MP, Kirschner MW. 2007. The relationship between
761 evolutionary and physiological variation in hemoglobin. *Proceedings of the National Academy of*
762 *Sciences* **104**: 16998–17003.
- 763 48. Lewis M, Chang G, Horton NC, Kercher MA, Pace HC, Schumacher MA, Brennan RG, Lu P.
764 1996. Crystal structure of the lactose operon repressor and its complexes with DNA and inducer.
765 *Science* **271**: 1247–54.
- 766 49. Moon TS, Lou C, Tamsir A, Stanton BC, Voigt CA. 2012. Genetic programs constructed from
767 layered logic gates in single cells. *Nature* **491**: 249–253.
- 768 50. Lutz R, Bujard H. 1997. Independent and tight regulation of transcriptional units in *Escherichia*
769 *coli* via the LacR/O, the TetR/O and AraC/I1-I2 regulatory elements. *Nucleic acids research* **25**:
770 1203–10.
- 771 51. Saiz L, Vilar JMG. 2008. *Ab initio* thermodynamic modeling of distal multisite transcription
772 regulation. *Nucleic Acids Research* **36**: 726.
- 773 52. Tungtur S, Skinner H, Zhan H, Swint-Kruse L, Beckett D. 2011. *In vivo* tests of thermodynamic
774 models of transcription repressor function. *Biophysical Chemistry* **159**: 142–151.
- 775 53. Forsén S, Linse S. 1995. Cooperativity: over the Hill. *Trends in Biochemical Sciences* **20**: 495 -
776 497.

- 777 54. Rosenfeld N, Young JW, Alon U, Swain PS, Elowitz MB. 2005. Gene regulation at the single-cell
778 level. *Science* **307**: 1962–1965.
- 779 55. Sourjik V, Berg HC. 2002. Receptor sensitivity in bacterial chemotaxis. *Proceedings of the National
780 Academy of Sciences of the United States of America* **99**: 123–127.
- 781 56. Eldar A, Elowitz M. 2010. Functional roles for noise in genetic circuits. *Nature* **467**: 167–173.
- 782 57. Gerland U, Hwa T. 2002. On the selection and evolution of regulatory DNA motifs. *Journal of
783 Molecular Evolution* **55**: 386–400.
- 784 58. Berg J, Willmann S, Lässig M. 2004. Adaptive evolution of transcription factor binding sites.
785 *BMC Evolutionary Biology* **4**: 42.
- 786 59. Zeldovich KB, Shakhnovich EI. 2008. Understanding protein evolution: from protein physics to
787 Darwinian selection. *Annual Review of Physical Chemistry* **59**: 105–127.
- 788 60. Sharan SK, Thomason LC, Kuznetsov SG, Court DL. 2009. Recombineering: a homologous
789 recombination-based method of genetic engineering. *Nature Protocols* **4**: 206–223.
- 790 61. Salis HM, Mirsky EA, Voigt CA. 2009. Automated design of synthetic ribosome binding sites to
791 control protein expression. *Nature Biotechnology* **27**: 946–950.
- 792 62. Thomason LC, Costantino N, Court DL. 2007. *E. coli* genome manipulation by P1 transduction.
793 *Current protocols in molecular biology* **Chapter 1**: Unit 1.17–1.17.8.
- 794 63. Fernández-Castané A, Vine CE, Caminal G, López-Santín J. 2012. Evidencing the role of lactose
795 permease in IPTG uptake by *Escherichia coli* in fed-batch high cell density cultures. *Journal of
796 Biotechnology* **157**: 391–398.
- 797 64. Maecker HT, Rinfret A, D’Souza P, Darden J, Roig E, Landry C, Hayes P, Birungi J, Anzala O,
798 Garcia M, et al.. 2005. Standardization of cytokine flow cytometry assays. *BMC Immunology* **6**:
799 13.
- 800 65. Aghaeepour N, Finak G, The FlowCAP Consortium, The DREAM Consortium, Hoos H, Mosmann
801 TR, Brinkman R, Gottardo R, Scheuermann RH. 2013. Critical assessment of automated flow
802 cytometry data analysis techniques. *Nature Methods* **10**: 228–238.
- 803 66. Lo K, Brinkman RR, Gottardo R. 2008. Automated gating of flow cytometry data via robust
804 model-based clustering. *Cytometry Part A* **73A**: 321–332.